Strong impact of wildfires on the abundance and aging of black carbon in the lowermost stratosphere

Jeannine Ditas[a,b], Nan Ma[a,b], Yuxuan Zhang[c], Denise Assmann[d], Marco Neumaier[e], Hella Riede[f,1], Einar Karu[f], Jonathan Williams[f], Dieter Scharffe[f], Qiaoqiao Wang[a], Jorge Saturno[c,g,2], Joshua P. Schwarz[h], Joseph M. Katich[h,i], Gavin R. McMeeking[j], Andreas Zahn[e], Markus Hermann[d], Carl A. M. Brenninkmeijer[f], Meinrat O. Andreae[g,k,l], Ulrich Pöschl[c], Hang Su[a,c,3], and Yafang Cheng[b,3]

[a]Center for Air Pollution and Climate Change Research (APCC), Jinan University, 510632 Guangzhou, China; [b]Minerva Research Group, Max Planck Institute for Chemistry, 55128 Mainz, Germany; [c]Multiphase Chemistry Department, Max Planck Institute for Chemistry, 55128 Mainz, Germany; [d]Experimental Aerosol and Cloud Microphysics, Leibniz Institute for Tropospheric Research, 04318 Leipzig, Germany; [e]Institute of Meteorology and Climate Research (IMK) - Atmospheric Trace Gases and Remote Sensing (ASF), Karlsruhe Institute of Technology, 76344 Eggenstein-Leopoldshafen, Germany; [f]Atmospheric Chemistry Department, Max Planck Institute for Chemistry, 55128 Mainz, Germany; [g]Biogeochemistry Department, Max Planck Institute for Chemistry, 55128 Mainz, Germany; [h]Chemical Sciences Division, National Oceanic and Atmospheric Administration Earth System Research Laboratory, Boulder, CO 80305; [i]Cooperative Institute for Research in Environmental Sciences, University of Colorado, Boulder, CO 80309; [j]Handix Scientific LLC, Boulder, CO 80301; [k]Scripps Institution of Oceanography, University of California, San Diego, La Jolla, CA 92037; and [l]Geology and Geophysics Department, King Saud University, Riyadh 11451, Saudi Arabia

Edited by Dennis L. Hartmann, University of Washington, Seattle, WA, and approved October 18, 2018 (received for review April 24, 2018)

Wildfires inject large amounts of black carbon (BC) particles into the atmosphere, which can reach the lowermost stratosphere (LMS) and cause strong radiative forcing. During a 14-month period of observations on board a passenger aircraft flying between Europe and North America, we found frequent and widespread biomass burning (BB) plumes, influencing 16 of 160 flight hours in the LMS. The average BC mass concentrations in these plumes (~140 ng·m^{-3}, standard temperature and pressure) were over 20 times higher than the background concentration (~6 ng·m^{-3}) with more than 100-fold enhanced peak values (up to ~720 ng·m^{-3}). In the LMS, nearly all BC particles were covered with a thick coating. The average mass equivalent diameter of the BC particle cores was ~120 nm with a mean coating thickness of ~150 nm in the BB plume and ~90 nm with a coating of ~125 nm in the background. In a BB plume that was encountered twice, we also found a high diameter growth rate of ~1 nm·h^{-1} due to the BC particle coatings. The observed high concentrations and thick coatings of BC particles demonstrate that wildfires can induce strong local heating in the LMS and may have a significant influence on the regional radiative forcing of climate.

black carbon | biomass burning | climate change | high altitude | mixing state

Extended summer dry seasons, drier vegetation, and decreased winter precipitation driven by climate change are leading to more frequent wildland fires in many parts of the world, with an increased duration and severity of burning (1–3). Especially in the northern high latitudes, where there is less intensive land management, a post-1750 increase in biomass burning (BB) events has been observed using the charcoal accumulation in sediments (charcoal index increased by ~0.4) (4). Wildland fires release large amounts of greenhouse gases, aerosol precursors, and primary aerosols including black carbon (BC) (5–7). Via deep convective clouds and synoptic weather systems associated with warm conveyor belts, a fraction of these emissions can be transported into the upper troposphere (UT) (8–12) and lowermost stratosphere (LMS) (13–16). At these high altitudes, BC particles can have a much stronger (up to ~10 times) radiative forcing efficiency than at lower altitudes (17–22) due to less-attenuated solar radiation, increased radiation from the backscattering of clouds, and longer residence time (23, 24). Moreover, an increasing BC concentration near the tropopause (TP) can also alter the vertical temperature profile, leading to a stabilizing effect in the atmosphere below, and can influence cloud and precipitation development in lower layers, resulting in a negative forcing contribution (22, 25).

High concentrations of refractory BC (rBC) (26) particles have been reported in BB plumes at altitudes of 10–12 km over northeast Germany (13) and at altitudes up to 7 km in the Arctic (27, 28). A BB plume observed over Germany in September 2011 exhibited elevated mass concentrations of rBC particles [up to 670 ng·m^{-3} at standard temperature and pressure (STP)] (13). This is nearly a two orders of magnitude increase in mass

Significance

Unique information about the abundance and evolution of wildfire-emitted black carbon (BC) in the lowermost part of the stratosphere (LMS) was obtained from long-term airborne measurements made in cooperation with Lufthansa through the Civil Aircraft for the Regular Investigation of the atmosphere Based on an Instrument Container (CARIBIC) project, part of the In-service Aircraft for a Global Observing System (IAGOS) framework. Our results demonstrate that wildfires can dramatically increase BC mass concentration in the LMS, substantially enhance regional climate forcing, and are a challenge for model simulations. Climate change is expected to increase the frequency and spread of wildfires. Thus, recording a present-day baseline with extensive and long-term measurements should help to constrain model estimations of the climate impact of BC and foster our fundamental understanding of future climate change.

Author contributions: H.S. and Y.C. designed research; J.D., N.M., H.S., and Y.C. performed research; N.M., H.S., and Y.C. contributed new reagents/analytic tools; J.D., N.M., Y.Z., D.A., M.N., H.R., E.K., J.W., D.S., Q.W., J.S., J.P.S., J.M.K., G.R.M., A.Z., M.H., C.A.M.B., M.O.A., U.P., H.S., and Y.C. analyzed data; and J.D., H.S., and Y.C. wrote the paper.

The authors declare no conflict of interest.

This article is a PNAS Direct Submission.

Data deposition: Data supporting the findings of this study are available at https://sites.google.com/view/jnu-apcc/downloads/pnas-2018-data, www.caribic-atmospheric.com/Data.php, and https://espoarchive.nasa.gov/archive/browse/atom. The LEO code for analyzing coating thickness of rBC from SP2 raw data are available at https://sites.google.com/view/jnu-apcc/downloads/mpic-sp2-toolkit.

[1]Present address: Department of Research and Development, Central Meteorological Application Development, Remote Sensing Application Development, Deutscher Wetterdienst, 63067 Offenbach am Main, Germany.

[2]Present address: Analytical Chemistry of the Gas Phase, Physikalisch-Technische Bundesanstalt, D-38116 Braunschweig, Germany.

[3]To whom correspondence may be addressed. Email: yafang.cheng@mpic.de or h.su@mpic.de.

This article contains supporting information online at www.pnas.org/lookup/suppl/doi:10.1073/pnas.1806868115/-/DCSupplemental.

Published online November 26, 2018.

ENVIRONMENTAL SCIENCES

concentration compared with high-altitude rBC measurements above the remote Pacific (29). Although these previous measurements in the BB plumes are snapshots at similar altitudes but in different regions, the high mass concentrations suggest a potentially strong climate impact of BB-derived rBC particles in the UT/LMS (22, 25). However, because of the lack of global observations of BC abundance and physicochemical properties (e.g., mixing state) at these altitudes (30, 31), large uncertainties still exist in the quantitative assessment of the global climate impact of BB-derived BC particles at high altitudes.

In August 2014, as part of the Civil Aircraft for the Regular Investigation of the atmosphere Based on an Instrument Container (CARIBIC) project [part of the In-service Aircraft for a Global Observing System (IAGOS) European Research Infrastructure] (32), a modified single-particle soot photometer (SP2) was integrated into the instrumented airfreight container onboard a Deutsche Lufthansa Airbus A340-600 airplane, allowing long-term measurements of rBC abundance, size, and mixing state in the midlatitude UT/LMS and the tropical free troposphere, mostly at an altitude of ∼10–12 km (*Methods*). From its integration until October 2015, the CARIBIC-SP2 made these measurements during more than 230 flight hours between Europe and North America, including ∼160 h in the LMS. Here, using this unique and extensive in situ dataset, we demonstrate the strong impact of BB emissions on the key climate-relevant properties of rBC particles at high altitude in the LMS.

Results

Concentration and Distribution. Strong spatial heterogeneity of rBC mass concentrations (M_{rBC}) was found in the LMS between Europe and North America based on the 14-mo period of observations (Fig. 1). To assess the influence of BB, we classified the air masses into three categories, namely background air, BB-affected air, and BB plume air, according to the examination of concurrent measurements of CO and acetonitrile (CH_3CN) (*Methods*). During 22 flights between Munich and San Francisco, between Munich and Los Angeles, and between Munich and Mexico City (for detailed flight information see *SI Appendix*, section S14 and Table S6), we frequently encountered enhanced M_{rBC} and rBC number concentrations (N_{rBC}) during flight segments with concurrently elevated CO and CH_3CN concentrations (Fig. 2 and *SI Appendix*, section S1 and Fig. S1). In total, more than 10% of the measurements in the LMS (∼16 of 160 h) were influenced by BB, with BB plumes and BB-affected air observed in 2.5% and 8% of the measurement time, respectively.

Compared with LMS background air [mean M_{rBC} = ∼6 ng·m^{-3} and N_{rBC} = ∼4.5 cm^{-3}, CO = ∼46 parts per billion (ppb), CH_3CN = ∼173 parts per trillion (ppt); gray dots in Fig. 2], different degrees of elevated pollutant concentrations have been found in BB plumes (mean M_{rBC} = ∼140 ng·m^{-3} and N_{rBC} = ∼48 cm^{-3}, CO = ∼158 ppb, CH_3CN = ∼463 ppt; yellow dots in Fig. 2) and in BB-affected air (mean M_{rBC} = ∼24 ng·m^{-3} and N_{rBC} = ∼11 cm^{-3}, CO = ∼87 ppb, CH_3CN = ∼232 ppt; purple dots in Fig. 2) (*SI Appendix*, Table S7). All aerosol (including rBC) mass and number concentrations mentioned in this study have been converted to STP [273.15 K and 1,013.25 hectopascal (hPa)]. The most intensive BB plumes were observed mainly in July and August, with the M_{rBC} reaching up to 720 ng·m^{-3} and major enhancements extending over 120–750 km. During transport in the LMS, BB plume air became mixed with background air, leading to even larger areas of influence (BB-affected air masses); for example, segments of 500–1,000 km were affected during flights 472 and 473 (*SI Appendix*, Table S6).

The potential vorticity (PV)-based vertical profiles of M_{rBC} and CO further demonstrate the influence of BB from the UT through the TP and into the LMS (*Methods*). As shown in Fig. 3, in three exemplary flights with intensive BB plumes, we observed concurrently increased CO and M_{rBC} values distributed either in the LMS (flights 472 and 473) or along the whole vertical profile in the UT/LMS and TP region (flight 515). In these regions, the CO concentration increased up to eightfold (from 50 to 400 ppb), while the M_{rBC} increased by a factor of 3 (from ∼250 to 720 ng·m^{-3}).

The strong contributions of BB plumes and BB-affected air to the statistical distribution of M_{rBC}, CO, and CH_3CN in the LMS are illustrated in Fig. 4. Here, to show the influence on the average concentration, we weighted the frequency distribution (*SI Appendix*, Fig. S2) by the corresponding concentration, and the integral in Fig. 4 thus represents the relative contributions of different air masses to loadings. While BB plumes (yellow area) are responsible for the second prominent peak (∼250 ng·m^{-3}) in the distribution of M_{rBC}, BB-affected air mass (purple area) influences mostly the middle range between background air (gray shading) and BB plumes (Fig. 4*A*). Due to the influence of BB, the regional mean M_{rBC} in all air masses (background air + BB-affected air + BB plumes) was increased by 75%, reaching an average value of 10.5 ng·m^{-3} compared with the average value of 6 ng·m^{-3} in background air. In contrast, the influence of BB

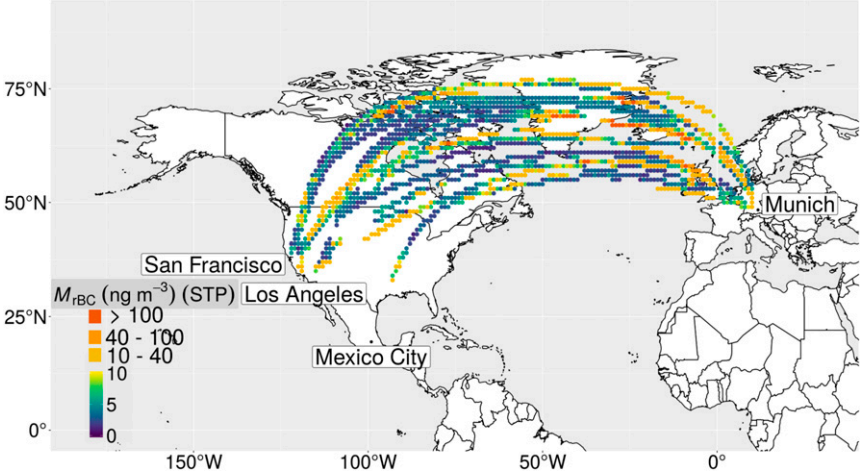

Fig. 1. Spatial distribution of M_{rBC} between Europe and North America in the LMS as obtained by 22 CARIBIC flights flying between Munich and San Francisco, between Munich and Los Angeles, and between Munich and Mexico City from August 2014 through October 2015. Flights mainly cover the region of 123.75°W–11.25°E and 35°N–77°N. The M_{rBC} data have been converted to STP conditions (273.15 K, 1,013.25 hPa) on a 1° × 1° grid.

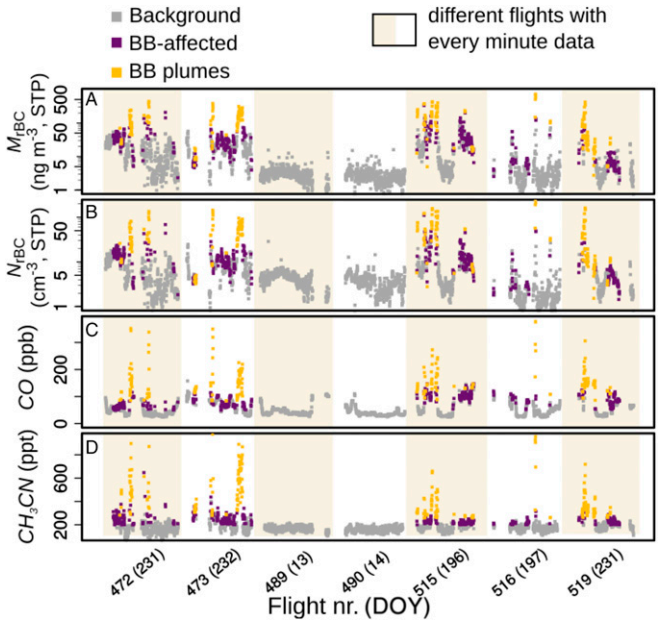

Fig. 2. Time series of observed M_{rBC} (*A*), N_{rBC} (*B*), CO mixing ratio (*C*), and CH_3CN mixing ratio (*D*) for seven IAGOS-CARIBIC flights. Individual flights are marked with white or pale yellow backgrounds. The whole dataset is divided into three air-mass regimes: (*i*) background (gray dots), (*ii*) BB-affected air (purple dots), and (*iii*) BB plumes (yellow dots). The numbers in brackets on the *x* axis show the day of the year (DOY). The complete series of 22 flights is shown in *SI Appendix*, Fig. S2.

emissions on the mixing ratios of CO and CH_3CN is less dramatic (Fig. 4 *B* and *C*), because their longer lifetimes (33, 34) lead to higher background levels.

The abundance of BC-containing particles relative to total aerosols is important for understanding the fate and radiative effect of aerosol particles. Fig. 5 shows the ratios of M_{rBC} (left) and N_{rBC} (right) relative to all aerosol particles for the three air mass types. The background rBC mass fraction of ∼0.4% in our study is consistent with measurements in the High-Performance Instrumented Airborne Platform for Environmental Research (HIAPER) Pole-to-Pole Observations (HIPPO) campaign, where an rBC mass fraction of <0.3% was reported above the TP (30, 35). The BB influence leads to an increase in number fraction of rBC-containing particles (∼1.5 times above background in the BB plume, Fig. 5) and in the size of rBC cores (from a mean diameter of ∼90 nm in background air to ∼120 nm in BB plumes) (Fig. 6*B*). However, the increase in rBC mass fraction was found only in the transition from background air to BB-affected air and did not extend further to the BB plumes. The M_{rBC} in BB plumes was more than five times higher than in BB-affected air, and an even stronger enhancement occurred in total aerosol mass. In an extreme case, the total aerosol extinction coefficient reached at least ∼120 Mm^{-1} in the LMS (*SI Appendix*, section S3), about four to five times higher than observed at this altitude over Europe after the Pinatubo volcanic eruptions in 1991 (16, 36). As shown in Fig. 6, BB plumes are characterized by high concentrations of larger non-BC particles and more thickly coated rBC particles. These particles, which contain more non-BC materials, can be removed efficiently in the transition from the BB plume to BB-affected air, as reflected by the reduced abundance of large aerosol particles and thickly coated rBC particles, thus leading to a higher rBC mass fraction in BB-affected air.

Mixing State. The light-absorption properties (37) and ice nucleation efficiency (38, 39) of rBC depend strongly on its mixing state, i.e., whether rBC is externally mixed (bare rBC particles surrounded by different aerosol particles) or internally mixed (an rBC core associated with other compounds, here referred to as "coatings" for simplicity). We set a minimum coating thickness of 30 nm as a threshold above which rBC particles were considered to be internally mixed (coated) (see *Methods* and *SI Appendix*, Figs. S4–S6 for details). In the LMS, we mainly find internally mixed rBC particles, especially in BB plumes. The fraction of coated rBC particles varied from ∼90% in background air to ∼95% in BB-affected air and reached 100% in BB plumes. The finding of very large fractions of coated rBC particles based on long-term statistics challenges the assumption of externally mixed BC particles used in previous model studies (22, 25) that assessed the radiative forcing of BC at high altitudes.

Fig. 7 shows the coating-thickness distribution of rBC-containing particles in the three different air masses. Besides a higher fraction of coated rBC particles, BB plumes clearly show thicker coatings with larger rBC cores. The mean coating thickness of rBC particles is ∼150 nm in BB plumes, higher than the thickness of ∼130 nm in BB-affected air mass and ∼125 nm in background air (*SI Appendix*, Fig. S7*A*). The percentage of coated rBC particles (∼90–100%) and the coating thicknesses (∼125–150 nm) we observed in the LMS are much larger than those measured in fresh BB emissions and in the boundary layer (9–70% and 20–65 nm) (6), pointing to a longer/stronger aging process during the long-range transport in the LMS.

The impact of BB emissions on background air is also evident from the coating-thickness distribution of rBC particles (Fig. 7). In background air, we observe two clusters overlapping at rBC core diameters of about 100–150 nm and coating thickness between 60 and 90 nm. The upper cluster (the second region of high probability density of data points located above the first one, Fig. 7, *Left*) gains importance with increasing BB influence and is shifted to larger coating thickness (Fig. 7, *Center* and *Right*). Mode fitting shows that among the multiple modes in background air, the thickly coated modes at ∼110 nm, ∼165 nm, and ∼220 nm coincide with the prominent modes in BB plumes and BB-affected air (*SI Appendix*, section S5 and Fig. S8). Surprisingly, these modes (110–220 nm), which were always observed in the LMS, were much less visible in the UT air, and the most thickly coated mode (∼220 nm) was actually diminished (*SI*

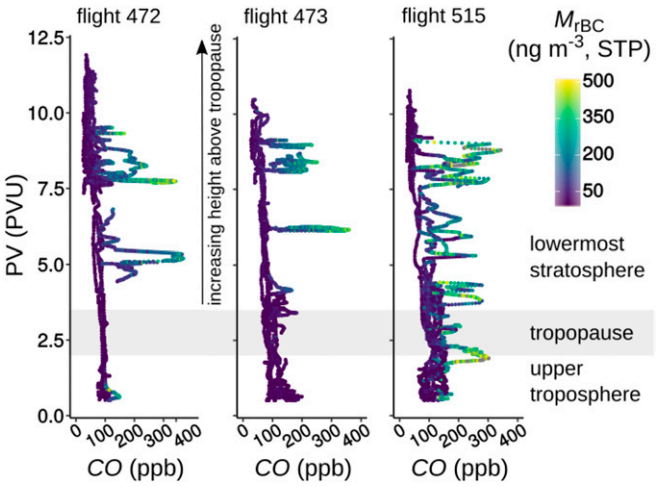

Fig. 3. PV-based vertical profiles of CO along the flight tracks Munich ↔ San Francisco (flights 472 and 473) and from Munich to Los Angeles (flight 515). The color coding shows the rBC loadings as M_{rBC}. The gray shading indicates the TP; the area below is classified as UT, and the area above is classified as LMS.

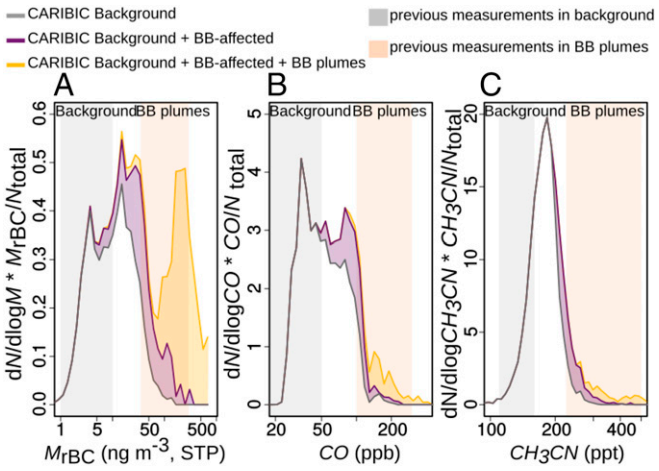

Fig. 4. Concentration-weighted frequency distributions of M_{rBC} (*A*), CO (*B*), and CH_3CN (*C*) for background air (gray), BB-affected air (purple), and BB plumes (yellow). The gray and light red shaded boxes represent the corresponding concentration ranges for background and BB plumes in the UT/LMS observed by previous studies (refs. 8, 9, 13, 27, 30, and 59–61; see also *SI Appendix*, sections S2 and S14, Fig. S2, and Table S7).

Appendix, Fig. S8). This suggests that a weaker removal process and a longer lifetime of rBC particles in the LMS than in the UT allows the formation of thicker coatings around rBC particles. We have also compared our coating statistics in the UT with those obtained over the Atlantic in a matched-latitude band during Atmospheric Tomography (ATom) missions 1 and 2 (*SI Appendix*, section S6). As shown in *SI Appendix*, Fig. S9, although the ATom result had poorer statistics due to fewer flight hours, it fits well within the range of our CARIBIC data, indicating a good agreement between the two datasets for background air masses in the UT. Besides the thickly coated modes, we also found a prominent mode in the LMS background air with a relatively thin coating of ∼50 nm (Fig. 7), whose contribution is, however, very small in the BB plume air (*SI Appendix*, Fig. S8). This mode and the noncoated rBC particles may be attributed mainly to fuel combustion, which has been suggested to contribute the major fraction of the LMS rBC burden (31), but the influence of aviation emissions cannot be excluded (24).

Aging and coating processes are often caused by the formation of secondary aerosols (40, 41). While aging in the LMS, aerosol particles accrete additional materials via condensation and coagulation. As shown in Fig. 6*A*, in BB plumes the number size distribution of coated rBC particles shows a vast increase, from 200–300 nm in background air, to ∼600 nm. This is caused mainly by the increasing coating thickness in BB plumes (Fig. 7 and *SI Appendix*, Fig. S7*A*), with a minor contribution from the increase in the rBC core diameter from ∼57 nm in background air to ∼100 nm in BB plumes (Fig. 6*B*). Since BB plumes increase the coating of rBC particles through a longer/stronger aging process, we may expect a similar growth in non-rBC particles and an increase in the secondary aerosol components. As shown in Fig. 6*C*, our measurements in LMS BB plumes show a count median diameter of ∼350 nm for total aerosol particles (mainly non-BC particles), which is much larger than the diameter of ∼100–160 nm observed in fresh smoke (42), thus demonstrating a strong aging process in the LMS. Moreover, the aerosol number size distribution developed an additional tail toward larger diameters (greater than ∼600 nm) with increasing BB influence; this is more obvious from the volume distribution in Fig. 6*D*. This tail includes the very thickly coated rBC particles in addition to the general increased size and number of aerosol particles in BB plumes.

Aging in an LMS-BB Plume. The repeated deployment of the CARIBIC laboratory enabled a rare observation of the aging of a BB plume. Flights 472 and 473 (Munich ↔ San Francisco) happened to intersect the same section of a large wildfire BB plume separated by ∼18 h of aging. This case allows us to quantify the changes in rBC microphysics in the course of the air-mass transport between the two encounters.

As shown in Fig. 8 (red dots), the revisited smoke plume had its origin in intensive fires in the Northwest Territories of Canada in July and August 2014 (https://modis.gsfc.nasa.gov/data/dataprod/mod14.php, accessed August 2018). The long trail of smoke was observed by the Aqua and Terra satellites on 17 August, 2014 (Fig. 8, *Top Left* satellite picture). In transit over Hudson Bay and Baffin Bay toward Greenland, the smoke plume was still spotted by the Aqua and Terra satellites on 20 August 2014 (Fig. 8, *Upper Right* satellite picture). The large-scale circulation is shown on the 250-hPa isobaric surface in *SI Appendix*, section S7 and Fig. S10. The forward trajectories show air-mass transport from the fire region at the surface to just below the TP. Although the backward trajectories stay above the TP and the actual mixing across the TP is not well represented, there is little doubt about the origin of the rBC intercepted during both flights. The back-trajectory–based time difference between the two plume visits is 16–19 h, which matches well the time elapsed between the respective flights (∼18 h). The aircraft data as well as the trajectories recorded an increase in plume altitude of 300 m between the two encounters.

Even far away from the wildfires, the BB plume exhibited an M_{rBC} of up to 300 ng·m^{-3} (Fig. 8, *Insets*), which was at least 50 times the M_{rBC} of background air. Both encounters with the plume show similar M_{rBC}-to-ΔCO ratios (ΔCO = plume CO – background CO), with averages of 1 and 1.3 ng·m^{-3}·ppb^{-1}, respectively. The rBC core-size distribution shows no growth during the transit time (25th and 75th percentages: ∼90–145 nm for both peaks), while the coating thickness of coated rBC particles increases by ∼5–7%. During the transit time of ∼18 h, the mean coating thickness increased from ∼160 nm for the first measurements in the plume (Fig. 9, light red color) to ∼170 nm for the second encounter with the BB plume (Fig. 9, light blue color). Hence, 77–96 h after emission, the growth rate of rBC

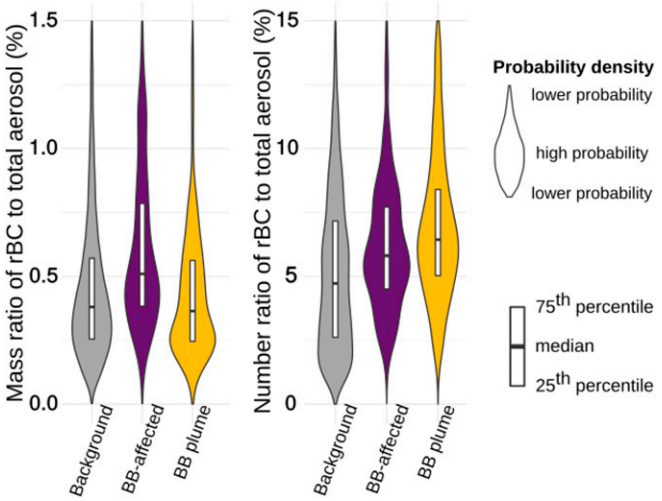

Fig. 5. M_{rBC} as a percentage of total accumulation-mode aerosol mass concentration (*Left*) and N_{rBC} as a percentage of total accumulation-mode aerosol number concentration (*Right*) in the three air-mass regimes: background, BB-affected air, and BB plumes. The white boxes mark the respective median values (middle lines) and the 25th and 75th percentile (top and bottom box edges). The shaded areas show the probability density of the three data populations.

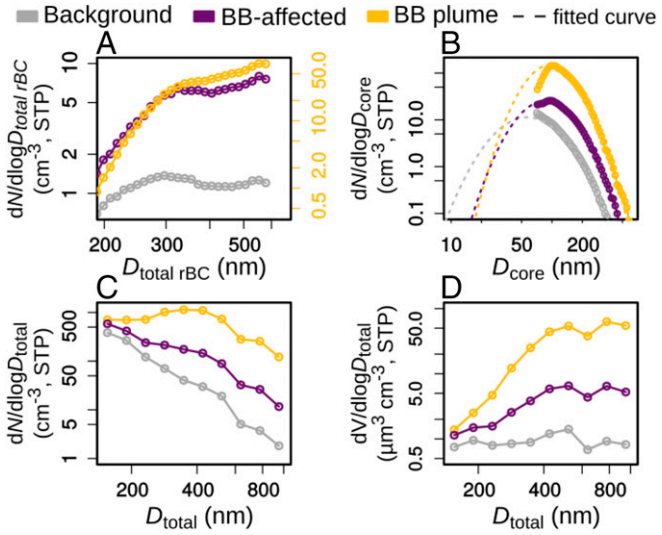

Fig. 6. Number size distributions of coated rBC particles (*A*), rBC cores (*B*), and all aerosol particles (*C*). (*D*) Volume distribution of all aerosol particles. D_{total} and D_{core} denote the particle diameter and rBC core diameter, respectively. The dashed lines are Gaussian distributions fitted to the mass distribution (shown in *SI Appendix*, section S3 and Fig. S3 *A*, *a*) and converted to the corresponding number distributions. Colors represent the three air-mass regimes.

particle diameters in this LMS BB plume is determined to be ~1 nm·h^{-1} (i.e., a 20-nm growth in diameter during the 18-h aging).

Due to their low volatility at low temperature, organics have been suggested to be important in particle formation and growth at high altitude (43, 44). Therefore, we investigated the possible contribution of organics to the coating process based on the concurrent measurements of volatile organic compounds (VOCs) (*Methods*). Accompanying the increase in coating thickness, we observed a 40% reduction in the measured VOC concentrations (here ethane, propane, i-butane, n-butane, n-pentane, benzene, and toluene). However, in addition to coating, both dilution and chemical processing can contribute to a reduction in VOCs. Given the corresponding 13.5 h of daylight, the degradation of VOCs by gas-phase chemistry is expected to be very small (except for a host of very short-lived VOCs that are not measured by CARIBIC). To explain the observed reduction in measured VOCs between the two encounters by gas-phase chemistry, an unrealistic 100-fold increase in OH would be needed (45, 46).

Assuming no chemical loss, the degree of VOC dilution could be as high as ~67% using mixing ratios of butane and propane measured for background air based on samples collected outside the plume. This calculation has uncertainties but indicates a significant mixing-in of background stratospheric air. At the same time, for more reactive volatile hydrocarbons and organic compounds, it is likely that chemical transformation and condensation occurred concomitant with this dilution. To estimate the scale of mass accumulation, we calculated the mass of gaseous carbon lost between the plume encounters. The respective values are 0.01 μg·m^{-3} for the measured C4–C7 nonmethane hydrocarbons and 0.32 μg·m^{-3} for C2–C7 compounds. Although some of these compounds may still be volatile at about −50 to −60 °C and at ~300 hPa in the LMS, they may be converted to low-volatility oxygenated compounds through heterogeneous oxidation and oligomerization reactions (44, 47). The measured increase in the size of rBC particles results in an estimated increase in the internally mixed mass of 0.06–0.11 μg·m^{-3}, assuming a growth of rBC particles with a core diameter between 120 nm and 340 nm and a density of 1,000 kg·m^{-3} for the condensed organic matter. If we assume the same rate of increase for the total aerosol population, noting that rBC particles constitute 6.6% of all aerosol particles in BB plumes in the LMS, then we estimate a total increase in aerosol mass of 1–1.7 μg·m^{-3}. This means that the reduction in organic compounds that we measured may account for up to 30% of the particle growth. It stands to reason to attribute the remaining fraction of observed growth to the condensation of oxidation products of VOCs and/or sulfuric acid present in the BB plume.

Discussion

High-altitude BC has a higher radiative forcing efficiency and can change the local thermal atmospheric structure (stability) and influence cloud covers (17–23). After reaching the LMS, BC has a longer lifetime, which further amplifies these effects. It is known that BB plumes interacting with strong convective systems can penetrate the TP and intrude into the stratosphere (8–10, 13, 15, 36, 48). However, because of limited measurements in the LMS, it is still not clear how frequently BB emissions can be transported and to what extent they influence the background BC levels. Our long-term measurement data provide strong evidence of frequent intrusion of BB emissions into the LMS between Europe and North America. Our data show that during the 14-mo period of observation, although only a modest 10% of the measurements were strongly influenced by BB, their contribution increased the regional mean M_{rBC} by 75% in the LMS. The observed contribution of 43% to the regional mean BC loadings at LMS by BB emissions is much stronger than previous model estimates of ~11–15% (*SI Appendix*, section S8) (31). In addition, the prominent thickly coated modes (~110- to 220-nm coating) in BB plumes also existed in background air, and thus we may expect a further contribution of BB to background levels. The large discrepancy between observations and model results seems to be caused mainly by the problem of representing wet scavenging and cross-TP transport in models, which limits BB intrusion into the LMS and prohibits the capture of the significant spread of high values of M_{rBC} found in this study.

The mixing state (coating thickness) of BC strongly regulates its radiative forcing, heating effect, and interactions with clouds, which in turn feed back to influence the fate of BC itself. It is not clear if the high-altitude BC, especially in the LMS, should have a thicker or thinner coating or even should be coated at all. On one hand, the low temperature and longer lifetime in the LMS favor a thicker coating due to the enhanced condensation of low-volatility compounds in colder environment. On the other hand, the low concentrations of particles and gaseous precursors and

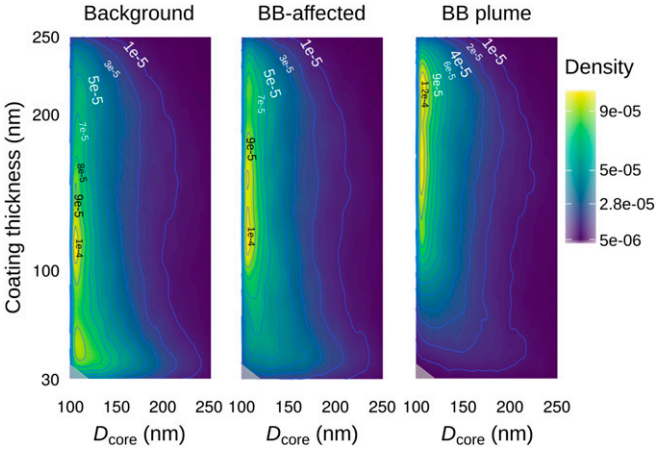

Fig. 7. Distribution of coating thickness of rBC particles at different core diameters for the three types of air mass. (*Left*) Background air. (*Center*) BB-affected air. (*Right*) BB plume air. The gray triangles denote rBC particles with a total particle size <180 nm.

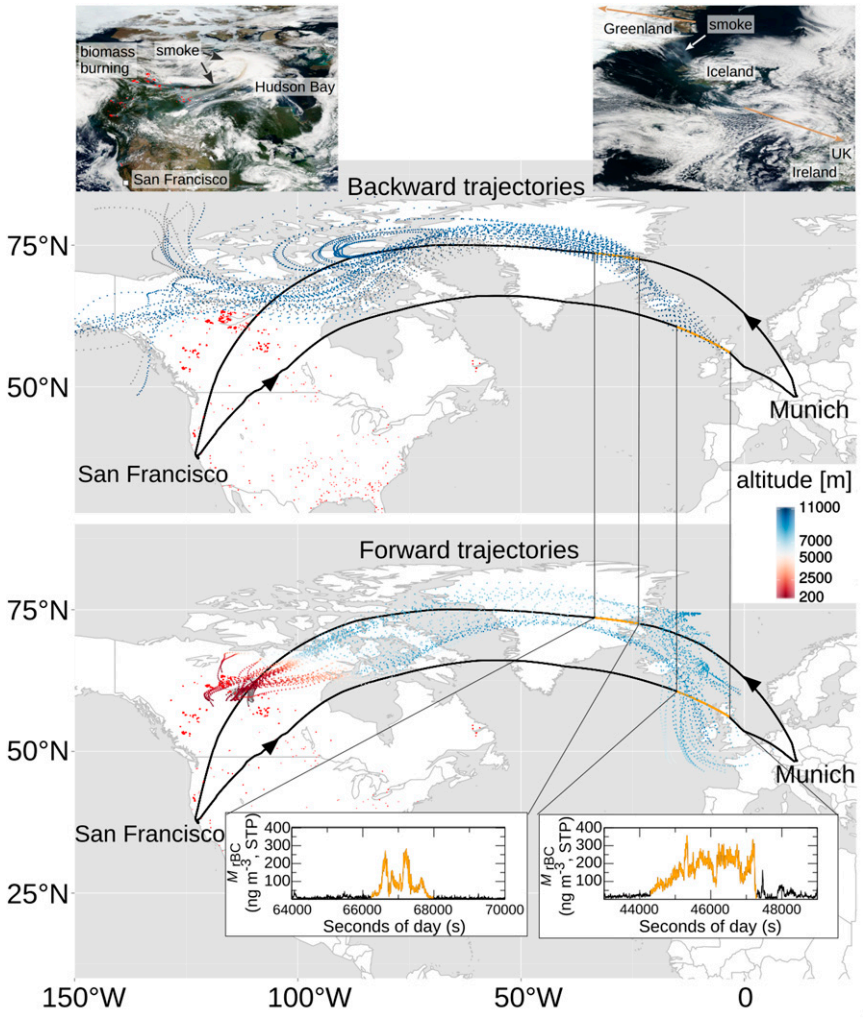

Fig. 8. Aging of rBC particles in an LMS-BB plume. Backward (77-h and 96-h) trajectories and the forward trajectories (88 h) for the marked flight segments (orange color in *Insets*) for the August 2014 flights. The color code denotes the altitude of the air mass. Smoke transported from the BB source area on 17 August 2014 over Greenland toward Iceland and the British Isles on 20 August 2014 was visualized in satellite imagery from MODIS Aqua Corrected Reflectance (True Color). Red dots mark fires and thermal anomalies obtained from MODIS Terra and Aqua (day and night). Satellite images courtesy of the NASA Worldview application (https://worldview.earthdata.nasa.gov/) operated by the NASA/Goddard Space Flight Center Earth Science Data and Information System (ESDIS) project.

low air pressure in the LMS may limit the coating processes. Moreover, the thickly coated aerosols are expected to be removed more efficiently during the upward transport to the LMS, and the impact of coating on ice nucleation makes the question even more complicated (38). Thus, the overall net effect on high altitude on rBC coating remains uncertain (16, 35). Our 14-mo measurements show that the overall net effect is a strong enhancement in coating thickness and in the much larger fraction of coated rBC particles in the LMS than in the source regions and in the boundary layer. This enhancement was observed not only in BB plumes but also in BB-affected and background air in the LMS. However, such strong enhancement was not found in the UT data. The lack of thick-coating modes (coating thickness of 110–210 nm) in the UT clearly shows the impact of the distinct removal processes and of BC lifetime on BC-coating processes in UT and LMS around the TP. In an LMS BB plume we observed a very fast growth rate ($\sim$1 nm·h^{-1}) for large accumulation-mode rBC particles, which is comparable to or even larger than the particle growth rate observed in polluted megacities (49).

The BB-induced enhancement of BC abundance and coating thickness may have a large impact on the BC heating rate and regional radiative forcing. Mie model calculations show that, compared with uncoated, bare BC, the lensing effect due to thick coating can enhance the absorption at a wavelength of 550 nm by $\sim$110% for background air and by 120% for BB plumes (*SI Appendix*, sections S9 and S10). To evaluate the effect of observed BB plumes on the regional radiative forcing and temperature structure, we applied a radiative transfer model, libRadtran (*SI Appendix*, section S3). The information about the vertical extent of BB plumes in the LMS from recent light detection and ranging (Lidar) measurement of Canadian wildfire smoke transported to Europe (16) was used here as a reference. We thus adopted a 1.5-km-thick plume layer in the LMS and a 5-km-thick BB emission-affected layer in the free troposphere. The aerosol concentrations (rBC plus scattering particles) in the 1.5-km layer were set as the observed average concentrations in background air, BB-affected air, and BB plumes. The aerosol optical thickness of the 5-km-thick layer was set as 50% of the 1.5-km-thick layer (*SI Appendix*, section S3), according to the observation of Ansmann et al. (16). To account for the lensing effect of the coating materials, the observed absorption-enhancement factors were applied for stratospheric and free tropospheric

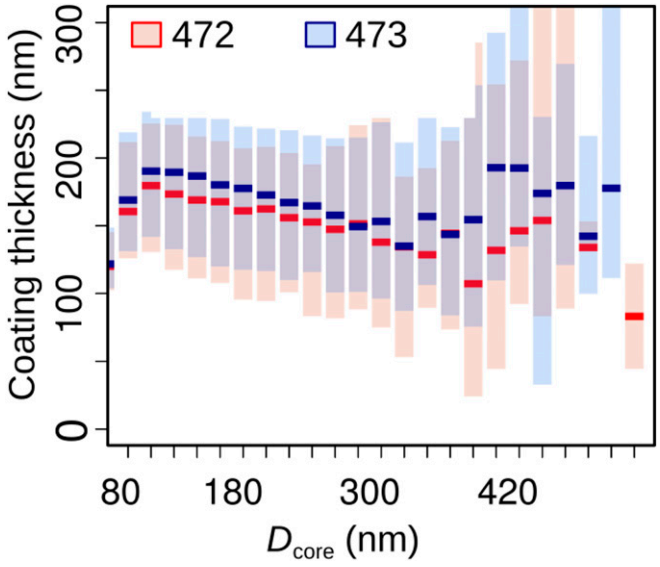

Fig. 9. Evolution of coating thickness for the range of core diameters of rBC particles between the two encounters of the BB plume intercepted by flights 472 and 473 (as shown in Fig. 8). The middle line denotes the median, and the box limits mark the 25th and 75th percentiles.

rBC particles, respectively (*SI Appendix*, section S10). The final influence of BB plumes and BB-affected air on the regional radiative forcing was scaled according to their occurrence, i.e., 2.5% and 8%, respectively. Our calculation shows that the observed BB plumes may lead to an ∼0.08 $W{\cdot}m^{-2}$ increase in the annual average of BC direct radiative forcing at the top of atmosphere in our observation region between Europe and North America. On one hand, the heating effect of BC will increase the air buoyancy and enhance the self-lifting of BB plumes in the LMS. On the other hand, it will form an inversion below the plumes, inhibiting the exchange between the UT and LMS. Based on our observations, we derived an ∼0.07 $K{\cdot}d^{-1}$ increase in the averaged heating rate attributed to BB plumes, which can reach ∼0.44 $K{\cdot}d^{-1}$ during extreme cases (*SI Appendix*, Table S4). The elevated amounts of rBC in the LMS are not limited to the Canadian and North American wildfires but are also expected to exist in other regions of strong BB (e.g., Siberia, Africa, South America, the Indian subcontinent, and southeast Asia) and with other kinds of BC emissions (24). Furthermore, our in situ observations and two recent Lidar- and remote sensing-based studies (15, 16) show that in extreme cases the elevation of total aerosol loading in the LMS due to the wildfires can be comparable to that of infrequent volcano eruptions. Considering the frequency of the intrusion during the fire seasons, wildfires may strongly influence the regional climate forcing and dynamic circulation at high altitude on seasonal and hemispheric scales (15).

Methods

IAGOS-CARIBIC Observatory. Our rBC measurements were performed with the IAGOS-CARIBIC observatory (www.iagos.org/iagos-caribic/). IAGOS-CARIBIC is a European Research Infrastructure that uses an instrumented airfreight container on board a Lufthansa Airbus A340-600 airplane (32). Measurement flights with different flight destinations covering an area from about 120°W to 120°E and 75°N to 30°S are carried out during four consecutive individual flights each month. A wide range of in situ measurements (CO, O_3, VOCs, greenhouse gases, H_2O, BC, and aerosol particles) is combined with the collection of air and aerosol samples for postflight laboratory analyses. In July/August 2014, the measurement container was modified to implement an SP2, allowing long-term rBC measurements in the midlatitude UT/LMS and the tropical free troposphere. The SP2 samples from a dedicated aerosol inlet. After its integration in the measurement container, the SP2 was used during more than 160 flight hours between Europe and North America, and these data are the focus of this study.

Here we also use concurrently measured data for CO and CH_3CN. Additionally, we use particle size distributions obtained with an optical particle size spectrometer (OPSS) (50), which detects accumulation-mode aerosol particles in the 0.14- to 1.05-μm diameter range. The CARIBIC OPSS (50) operations are conducted by the Leibniz Institute for Tropospheric Research (TROPOS). Nonmethane hydrocarbon (51) and greenhouse gas measurements (52) were made from pressurized air samples at the Max Planck Institute for Chemistry. The CO analyzer (53) is also operated by the Max Planck Institute for Chemistry. Acetone and CH_3CN were measured by a proton transfer reaction mass spectrometer (54) operated by the Karlsruhe Institute of Technology.

SP2. The SP2 instrument (Droplet Measurement Technologies) was modified to fulfill the complex requirements of automated start, measurement, and shut-down cycles for four consecutive long-range flights on board the Airbus A340-600 passenger aircraft and to comply with aircraft safety regulations. The SP2 was equipped with a software interface implemented to control the instrument via the CARIBIC master computer. The pumping system of the SP2 was adjusted to the pump system already existing in the measurement container. The SP2 instrument measures the size of non-rBC–containing aerosol particles (in the size range of 150–400 nm) based on scattered laser light and measures the mass of rBC (26) within single aerosol particles (in the size range of 70–600 nm assuming a 1.8 $g{\cdot}cm^{-3}$ void-free particle density for the rBC component) based on laser-induced incandescence (55). In the SP2, individual aerosol particles pass a Nd:YAG laser cavity perpendicularly. The surrounding detectors measure the scattered laser light of nonabsorbing aerosol particles and the scattered and incandescent light of BC-containing particles. BC-containing particles are heated to evaporation (∼4,000 K) during their passage through the laser beam. While the amount of scattered light of a nonabsorbing particle is proportional to its size, the amount of incandescent light emitted is proportional to the rBC mass within each individual aerosol particle. The SP2 was calibrated before each flight sequence with Fullerene soot (lot: L20W054) and polystyrene latex spheres between 150 and 350 nm in diameter. During the whole measurement period the laser power was stable at 5.3 eV.

The evaporation of the rBC particles within the laser beam complicates the interpretation of light scattering from these particles. However, the optical size of the original particle can be measured using the leading edge-only fit (hereafter called the "LEO method") (56). A detailed description of this method, including a schematic figure, is shown in *SI Appendix*, Fig. S14. In brief, the LEO method uses the combination of scattering and incandescence signals measured during the transit of an rBC particle through the laser beam. The incandescence signal is used to calculate the rBC core size, and the scattering signal contains information of the original particle optical size. This method was applied for each measured rBC-containing particle detected during the 22 flights. In the coating-thickness analysis we included only all rBC particles with a total optical particle size larger than 180 nm and a coating thickness larger 30 nm (∼1.3 million particles). This lower cutoff is at the fifth percentile of all calculated coating thicknesses (*SI Appendix*, Fig. S3).

Measurement Flights. Between August 2014 and October 2015, 22 flights were conducted with the CARIBIC observatory between Munich and San Francisco, Munich and Los Angeles, and Munich and Mexico City (Fig. 1). These flights reveal different conditions of BB aerosol. (Further information about the flights, including date and take-off and landing times, is given in *SI Appendix*, Table S1. Detailed meteorological information for all CARIBIC flights is available at projects.knmi.nl/campaign_support/CARIBIC/.) Our rBC measurements start at an altitude of 690 hPa (∼2- to 3-km altitude) to avoid contamination from the airport and potential turbulent flow conditions in the inlet sampling line. In the present study we concentrate on measurements performed in the LMS. For long-range transport of rBC particles, as observed for the measured BB smoke, the altitude is an important aspect. In the LMS, the lifetime of these particles is on the order of months, much longer than in the UT, where rBC particles survive for 1 d to 2 wk (23). This implies that in the rBC particles in the LMS can be transported and distributed over long distances (500–700 km) and wide areas.

As a measure of height above the TP, we use the PV calculated based on European Centre for Medium-Range Weather Forecasts reanalysis data with 1° resolution in latitude and longitude at the Royal Netherlands Meteorological Institute. One PV unit (PVU) equals 10^{-6} $km^2{\cdot}kg^{-1}{\cdot}s^{-1}$. For our aircraft flights at midlatitudes, a value >2 PVU is taken to denote the TP and the LMS region above it. For our study, we used only TP and LMS data to avoid tropospheric influence, and thus we analyzed only BB aerosol that underwent

long-range transport. Our analysis is based on ∼160 flight hours in the TP and LMS.

Air-Mass Classification. The 22 measurement flights exhibit different degrees of BB impact, which were delineated into three categories based on measurements of CO and CH_3CN. While CO is produced by incomplete combustion in general, CH_3CN is directly produced and emitted into the atmosphere almost exclusively during BB events (57, 58). In general, we observed three regimes of air masses: (*i*) background air, (*ii*) BB-affected air, and (*iii*) BB plumes. BB-influenced air-mass regimes are distinguished from background air masses by using Northern Hemispheric climatological background values for CO depending on the month, latitude, and PV based on ∼330 hours of CARIBIC flights performed between 2012 and 2016. The difference between the background and measured CO value (ΔCO) is used together with CH_3CN to discriminate between the different air-mass types. In BB-affected air masses the values of both parameters are larger than the 75th percentile of LMS data (CH_3CN = 199 ppt; ΔCO = 22 ppb), while BB plumes show extreme values exceeding the 95th percentile of LMS data (CH_3CN = 259 ppt; ΔCO = 56 ppb). Although the thresholds are somewhat arbitrary, the 75th percentile is consistent with the 99.9th percentile of the two cleanest flights. Additionally, the 75th percentile agrees with thresholds found in literature of CH_3CN >200 ppt for fire plumes (31) and for Canadian fires (ΔCH_3CN >100 ppt above background) (7). The frequency distributions of CH_3CN and ΔCO for all data in the LMS are given in *SI Appendix*, Fig. S15. As shown in Fig. 4, classification of background air and BB plumes in previous measurements in the UT/LMS (refs. 8, 9, 13, 27, 30, and 59–61, see also *SI Appendix*, sections S2 and S15, Fig. S2, and Table S8) fit in well in our distribution. Finally, we distinguish between the following three air-mass regimes:

i) Background air (denoted with gray color):
- The cleanest air encountered in our measurement period
- An actual CH_3CN concentration less than the 75th percentile of total CH_3CN (199 ppt)
- An actual CO concentration: ΔCO [ΔCO = measured CO concentration – background (depending on latitude, month, and PV height)] less than the 75th percentile of total ΔCO (22 ppb)

ii) BB-affected air (denoted with purple color):
- Mixture between background air and BB plumes
- Enhanced concentration of CH_3CN greater than the 75th percentile of total CH_3CN (199 ppt) and lower than the 95th percentile of total CH_3CN (259 ppt)
- Enhanced concentration of CO: ΔCO greater than the 75th percentile of total ΔCO (22 ppb) and lower than the 95th percentile of total ΔCO (56 ppb)

iii) BB plumes (denoted with yellow color):
- Fresh or aged BB plume
- Strongly enhanced concentration of CH_3CN greater than the 95th percentile of total CH_3CN (259 ppt)
- Strongly enhanced concentration of CO: ΔCO greater than the 95th percentile of total ΔCO (56 ppb)

ACKNOWLEDGMENTS. We thank NOAA Air Resources Laboratory (ARL) for providing the HYSPLIT transport and dispersion model and READY website (https://www.ready.noaa.gov/index.php). We acknowledge the use of imagery from the NASA Worldview application (https://worldview.earthdata.nasa.gov/) operated by the NASA/Goddard Space Flight Center (GSFC)/Earth Science Data and Information System (ESDIS) project. Special thanks go to Lufthansa, Lufthansa Technical Division, Munich Airport, and the entire IAGOS-CARIBIC team. We acknowledge the National Natural Science Foundation of China (91644218), National Key Research and Development Program of China (Grant 2017YFC0210104), and Guangdong Innovative and Entrepreneurial Research Team Program (2016ZT06N263). The German Federal Ministry of Education and Research (BMBF) provided financial support for the CARIBIC observatory operation as part of the Joint Project IAGOS-D. The German Research Foundation (DFG) provided financial support for OPSS data analysis within the Priority Program 1294 (HALO). This work was supported by the Max Planck Society (MPG). Y.C. also acknowledges the Minerva Program of MPG. J.D. gratefully acknowledges the joint postdoctoral program from Jinan University and the Max Planck Institute for Chemistry.

1. Westerling AL, Hidalgo HG, Cayan DR, Swetnam TW (2006) Warming and earlier spring increase western U.S. forest wildfire activity. *Science* 313:940–943.
2. Abatzoglou JT, Williams AP (2016) Impact of anthropogenic climate change on wildfire across western US forests. *Proc Natl Acad Sci USA* 113:11770–11775.
3. Crockett JL, Westerling AL (2018) Greater temperature and precipitation extremes intensify Western US droughts, wildfire severity, and Sierra Nevada tree mortality. *J Clim* 31:341–354.
4. Marlon JR, et al. (2009) Climate and human influences on global biomass burning over the past two millennia. *Nat Geosci* 2:307.
5. Andreae MO (1993) The influence of tropical biomass burning on climate and the atmospheric environment. *Biogeochem Global Change,* 113–150.
6. Schwarz JP, et al. (2008) Measurement of the mixing state, mass, and optical size of individual black carbon particles in urban and biomass burning emissions. *Geophys Res Lett* 35:L13810.
7. Kondo Y, et al. (2011) Emissions of black carbon, organic, and inorganic aerosols from biomass burning in North America and Asia in 2008. *J Geophys Res Atmos* 116: D08204.
8. Andreae MO, et al. (2001) Transport of biomass burning smoke to the upper troposphere by deep convection in the equatorial region. *Geophys Res Lett* 28:951–954.
9. Jost HJ, et al. (2004) In-situ observations of mid-latitude forest fire plumes deep in the stratosphere. *Geophys Res Lett* 31:L11101.
10. Fromm M, et al. (2008) Stratospheric impact of the Chisholm pyrocumulonimbus eruption: 2. Vertical profile perspective. *J Geophys Res Atmos* 113:D08203.
11. Cooper OR, et al. (2004) A case study of transpacific warm conveyor belt transport: Influence of merging airstreams on trace gas import to North America. *J Geophys Res* 109:D23S08.
12. Ding AJ, et al. (2009) Transport of north China air pollution by mid-latitude cyclones: A case study of aircraft measurements in summer 2007. *J Geophys Res* 114:D08304.
13. Dahlkötter F, et al. (2014) The Pagami Creek smoke plume after long-range transport to the upper troposphere over Europe–Aerosol properties and black carbon mixing state. *Atmos Chem Phys* 14:6111–6137.
14. Trentmann J, et al. (2006) Modeling of biomass smoke injection into the lower stratosphere by a large forest fire (part I): Reference simulation. *Atmos Chem Phys* 6: 5247–5260.
15. Peterson DA (2018) Wildfire-driven thunderstorms cause a volcano-like stratospheric injection of smoke. *Clim Atmos Sci* 1:30.
16. Ansmann A, et al. (2018) Extreme levels of Canadian wildfire smoke in the stratosphere over central Europe on 21–22 August 2017. *Atmos Chem Phys* 18: 11831–11845.
17. Haywood JM, Ramaswamy V (1998) Global sensitivity studies of the direct radiative forcing due to anthropogenic sulfate and black carbon aerosols. *J Geophys Res* 103: 6043–6058.
18. Houghton JT, et al. (1996) *Climate Change 1995: The Science of Climate Change, Contribution of Working Group I to the Second Assessment Report of the Intergovernmental Panel on Climate Change* (Cambridge Univ Press, Cambridge, UK).
19. Zarzycki CM, Bond T (2010) How much can the vertical distribution of black carbon affect its global direct radiative forcing? *Geophys Res Lett* 37:L20807.
20. Samset B, Myhre G (2011) Vertical dependence of black carbon, sulphate and biomass burning aerosol radiative forcing. *Geophys Res Lett* 38:L24802.
21. Samset BH, et al. (2013) Black carbon vertical profiles strongly affect its radiative forcing uncertainty. *Atmos Chem Phys* 13:2423–2434.
22. Ban-Weiss GA, Cao L, Bala G, Caldeira K (2012) Dependence of climate forcing and response on the altitude of black carbon aerosols. *Clim Dyn* 38:897–911.
23. Bond TC, et al. (2013) Bounding the role of black carbon in the climate system: A scientific assessment. *J Geophys Res Atmos* 118:5380–5552.
24. Govardhan G, Satheesh SK, Nanjundiah R, Moorthy KK, Babu SS (2017) Possible climatic implications of high-altitude black carbon emissions. *Atmos Chem Phys* 17: 9623–9644.
25. Samset BH, Myhre G (2015) Climate response to externally mixed black carbon as a function of altitude. *J Geophys Res Atmos* 120:2913–2927.
26. Petzold A, et al. (2013) Recommendations for reporting black carbon measurements. *Atmos Chem Phys* 13:8365–8379.
27. Warneke C, et al. (2009) Biomass burning in Siberia and Kazakhstan as an important source for haze over the Alaskan Arctic in April 2008. *Geophys Res Lett* 36:L02813.
28. Spackman JR, et al. (2010) Aircraft observations of enhancement and depletion of black carbon mass in the springtime Arctic. *Atmos Chem Phys* 10:9667–9680.
29. Schwarz JP, et al. (2006) Single-particle measurements of mid latitude black carbon and light-scattering aerosols from the boundary layer to the lower stratosphere. *J Geophys Res Atmos* 111:D16207.
30. Schwarz JP, et al. (2013) Global-scale seasonally resolved black carbon vertical profiles over the Pacific. *Geophys Res Lett* 40:5542–5547.
31. Wang Q, et al. (2014) Global budget and radiative forcing of black carbon aerosol: Constraints from pole-to-pole (HIPPO) observations across the Pacific. *J Geophys Res* 119:195–206.
32. Brenninkmeijer CAM, et al. (2007) Civil aircraft for the regular investigation of the atmosphere based on an instrumented container: The new CARIBIC system. *Atmos Chem Phys* 7:4953–4976.
33. Prinn RG (2003) The cleansing capacity of the atmosphere. *Annu Rev Environ Resour* 28:29–57.
34. Harrison JJ, Bernath PF (2013) ACE-FTS observations of acetonitrile in the lower stratosphere. *Atmos Chem Phys* 13:7405–7413.
35. Schwarz JP, et al. (2008) Coatings and their enhancement of black carbon light absorption in the tropical atmosphere. *J Geophys Res* 113:D03203.
36. Ansmann A, Mattis I, Wandinger U, Wagner F (1997) Evolution of the Pinatubo aerosol: Raman Lidar observations of particle optical depth, effective radius, mass, and surface area over Central Europe. *J Atmos Sci* 54:2630–2641.

37. Liu D, et al. (2017) Black-carbon absorption enhancement in the atmosphere determined by particle mixing state. *Nat Geosci* 10:184–188.
38. Hoose C, Möhler O (2012) Heterogeneous ice nucleation on atmospheric aerosols: A review of results from laboratory experiments. *Atmos Chem Phys* 12:9817–9854.
39. Targino AC, et al. (2009) Influence of particle chemical composition on the phase of cold clouds at a high-alpine site in Switzerland. *J Geophys Res Atmos* 114:D18206.
40. Cheng Y, et al. (2006) Mixing state of elemental carbon and non-light-absorbing aerosol components derived from in situ particle optical properties at Xinken in Pearl River Delta of China. *J Geophys Res* 111:D20204.
41. Cheng Y, et al. (2012) Size-resolved measurement of the mixing state of soot in the megacity Beijing, China: Diurnal cycle, aging and parameterization. *Atmos Chem Phys* 12:4477–4491.
42. Reid JS, Koppmann R, Eck TF, Eleuterio DP (2005) A review of biomass burning emissions part II: Intensive physical properties of biomass burning particles. *Atmos Chem Phys* 5:799–825.
43. Farina SC, Adams PJ, Pandis SN (2010) Modeling global secondary organic aerosol formation and processing with the volatility basis set: Implications for anthropogenic secondary organic aerosol. *J Geophys Res* 115:D09202.
44. Andreae MO, et al. (2018) Aerosol characteristics and particle production in the upper troposphere over the Amazon Basin. *Atmos Chem Phys* 18:921–961.
45. McKeen SA, Trainer M, Hsie EY, Tallamraju RK, Liu SC (1990) On the indirect determination of atmospheric OH radical concentrations from reactive hydrocarbon measurements. *J Geophys Res* 95:7493–7500.
46. Blake NJ, et al. (1993) Estimates of atmospheric hydroxyl radical concentrations from the observed decay of many reactive hydrocarbons in well-defined urban plumes. *J Geophys Res Atmos* 98:2851–2864.
47. Shiraiwa M, et al. (2011) The role of long-lived reactive oxygen intermediates in the reaction of ozone with aerosol particles. *Nat Chem* 3:291–295.
48. Fromm M, et al. (2010) The untold story of pyrocumulonimbus. *Bull Am Meteorol Soc* 91:1193–1209.
49. Wiedensoher A, et al. (2009) Rapid aerosol particle growth and increase of cloud condensation nucleus activity by secondary aerosol formation and condensation: A case study for regional air pollution in northeastern China. *J Geophys Res* 114: D00G08.
50. Hermann M, et al. (2016) An optical particle size spectrometer for aircraft-borne measurements in IAGOS-CARIBIC. *Atmos Meas Tech* 9:2179–2194.
51. Baker AK, Slemr F, Brenninkmeijer CAM (2010) Analysis of non-methane hydrocarbons in air samples collected aboard the CARIBIC passenger aircraft. *Atmos Meas Tech* 3:311–321.
52. Schuck TJ, Brenninkmeijer CAM, Slemr F, Xueref-Remy I, Zahn A (2009) Greenhouse gas analysis of air samples collected onboard the CARIBIC passenger aircraft. *Atmos Meas Tech* 2:449–464.
53. Scharffe D, Slemr F, Brenninkmeijer CAM, Zahn A (2012) Carbon monoxide measurements onboard the CARIBIC passenger aircraft using UV resonance fluorescence. *Atmos Meas Tech* 5:1753–1760.
54. Sprung D, Zahn A (2010) Acetone in the upper troposphere/lowermost stratosphere measured by the CARIBIC passenger aircraft: Distribution, seasonal cycle, and variability. *J Geophys Res Atmos* 115:D16301.
55. Stephens M, Turner N, Sandberg J (2003) Particle identification by laser-induced incandescence in a solid-state laser cavity. *Appl Opt* 42:3726–3736.
56. Gao RS, et al. (2007) A novel method for estimating light-scattering properties of soot aerosols using a modified single-particle soot photometer. *Aerosol Sci Technol* 41: 125–135.
57. Lobert JM, Scharffe DH, Hao WM, Crutzen PJ (1990) Importance of biomass burning in the atmospheric budgets of nitrogen-containing gases. *Nature* 346:552–554.
58. Holzinger R, et al. (1999) Biomass burning as a source of formaldehyde, acetaldehyde, methanol, acetone, acetonitrile, and hydrogen cyanide. *Geophys Res Lett* 26:1161–1164.
59. Baumgardner D, Kok G, Krämer M, Weidle F (2008) Meridional gradients of light absorbing carbon over northern Europe. *Environ Res Lett* 3:25010.
60. Schneider J, Bürger V, Arnold F (1997) Methyl cyanide and hydrogen cyanide measurements in the lower stratosphere: Implications for methyl cyanide sources and sinks. *J Geophys Res* 102:25,501–25,506.
61. Vay SA, et al. (2011) Patterns of CO2 and radiocarbon across high northern latitudes during international polar year 2008. *J Geophys Res* 116:D14301.